Validation of a Multiphase Model for the Macrosegregation and Primary Structure of High-Grade Steel Ingots

R. TANZER, W. SCHÜTZENHÖFER, G. REITER, H.-P. FAULAND, L. KÖNÖZSY, A. ISHMURZIN, M. WU, and A. LUDWIG

A mixed columnar-equiaxed solidification model is used to predict the macrosegregation in high grade steel ingots. In this model, three phases are considered: the melt; the columnar phase, which is assumed to be stationary; and the equiaxed phase, which is free to move. With this approach, the model is able to simulate the evolution of the primary solid phase distributions including the columnar-to-equiaxed transition, the melt convection and the grain sedimentation, and their influence on the macrosegregation. Thermodynamic information of a ternary alloy (Fe-C-Cr) is simplified by the piecewise linearization of the phase diagram around the suitable compositions in the ferritic and austenitic regions. As a result, macrosegregation of carbon and chromium has been analyzed. As the first step, the validation of the numerical model was performed on a benchmark ingot of a laboratory scale. Computed macrosegregation and primary structure were compared with measurements and good agreement was obtained.

I. INTRODUCTION

FOR the as-cast ingots of high grade steels, many rejection criteria are defined, which are critical for the downstream production chains such as rolling or forging. The most important criteria for the as-cast ingots are the macrosegregation of the major alloying elements, *e.g.*, carbon and chromium, and the inhomogeneous distribution of the primary structure (the columnar zone, the equiaxed zone, and the columnar-to-equiaxed transition). However, both macrosegregation and primary structure are strongly related to the process parameters such as the pouring temperature, the casting rate, the mold design, or the use of insulation or exothermic powder. In order to understand the impact of these process parameters on ingot quality, it is necessary to perform numerous casting trials, which are time consuming and costly. An alternative approach to optimize the process parameters is the use of multiphase and multicomponent modeling. Therefore, Böhler Edelstahl GmbH & Co KG (BEG), a renowned producer of tool steels and special materials, and the CD Laboratory for Multiphase Simulation of Metallurgical Processes (CDL), University of Leoben, started a

cooperation. The numerical models are developed at the CDL, whereas BEG produces ingots of different sizes to validate the model. The outcome of the cooperation will be a model to simulate the formation of macrosegregation and the evolution of primary structure in the as-cast state of ingots.

This article presents the preliminary results of applying the multiphase model for simulating solidification of a ternary steel (Fe-C-Cr) and compares the computed data with the laboratory scale casting experiment data.

Great efforts were made in the understanding of solidification and the formation of macrosegregation in steel.[1,2] On this basis, a number of articles have been published dealing with the prediction of macrosegregation of steel castings using numerical simulation.[3–5] Gu and Beckermann[6] used a model for solidification of a multicomponent steel with numerical solution of fully coupled mass, momentum, energy, and species conservation equations for the liquid and solid regions as well as the mushy zone. The model was applied to describe the macrosegregation and the flow pattern caused by thermal and solutal convection in a large steel ingot, and good agreement of predicted and actual center line segregations of carbon and sulfur was found. Kaempfer and Rappaz[7] presented a numerical method that used an adaptive finite element grid. The fixed coarse grid of the finite element mesh is used for computations on the casting scale, and a fine mesh, which is created by subdivision of the coarse elements, is used to describe the mushy zone. The simulations will be extended from two-dimensional and axisymmetric cases to the three-dimensional case with the advent of computational power. Cao *et al.*[8] considered a cubic casting with a cylindrical riser, taking into account thermosolutal convection during solidification. The simulation results for carbon concentrations were also in good agreement with experimental results. These models, however, are

R. TANZER, Researcher, W. SCHÜTZENHÖFER, Head of R&D Department, G. REITER, Production Assistant, Special Steel Plant, and H.-P. FAULAND, Head of Steel Plants, are with Böhler Edelstahl GmbH & Co KG (BEG), Kapfenberg, Austria. Contact e-mail: robert.tanzer@bohler-edelstahl.at L. KÖNÖZSY, A. ISHMURZIN, and M. WU, Researchers, and A. LUDWIG, Head, are with the Christian-Doppler Laboratory for Multiphase Modeling of Metallurgical Processes, Department of Metallurgy, University of Leoben (MUL), Leoben, Austria.

not able to predict the primary solidification structure, since they do not distinguish between the columnar and equiaxed phases that occur and interact with each other during solidification.

The present work is the validation of the recent development and application of the volume averaged multiphase/multicomponent (Fe-C-Cr) model by Ludwig et al.[9,10] and Wu et al.[11,12] The governing equations of the multiphase approach for solidification and melting processes were presented. The numerical results from a simulation of solidification of a ternary (Fe-C-Cr) alloy have been explained considering the process parameters such as the thermal and solutal convection and the nucleation parameters based on a parameter study by Könözsy et al.[13] The multicomponent modeling is one of the most relevant outcomes of the CDL and BEG cooperation coupling solidification kinetics with thermodynamics. This method was developed and implemented by Ishmurzin et al.[14]

II. MODEL DESCRIPTION AND THERMODYNAMICS

A. Modeling of the Mass-Transfer Rates

A volume averaged Eulerian–Eulerian multiphase solidification and melting model, which was developed for the binary system,[9] has been extended for the ternary system.[10,14] Three phases are considered in the corresponding conservation equations, namely, liquid-phase l, columnar dendrite trunks c, and equiaxed grains e. In order to define the mass-transfer rates for the equiaxed and columnar phases, it is necessary to model their kinetic growth behavior. The morphology of equiaxed grains is approximated by ideal spheres. The growth velocity of equiaxed grains can be analytically derived[7–9] as

$$v_{R_e} = \frac{2D_j}{d_e} \cdot \frac{\tilde{c}_l^j - c_l^j}{\tilde{c}_l^j - \tilde{c}_e^j} \quad [1]$$

where D_j is the diffusion coefficient of the jth species in the liquid; d_e is the diameter of equiaxed grains; c_l^j is the liquid mass fraction of the jth species; and $\tilde{c}_l^j$ and $\tilde{c}_e^j$ are the equilibrium species mass fractions at the liquid-solid interface. The j index is valid for all considered species in the multicomponent system (j = C and Cr for the ternary system in question).

Columnar dendrite trunks are assumed to be stationary, stick to the mold wall, and solidify toward the bulk melt; therefore, the momentum equation for the columnar phase is not solved. The columnar phase is approximated by cylinders. The distance between two cylinder centers represents the primary dendrite arm spacing for which a constant value is assumed. Their growth velocity can also be analytically derived[9–12] as

$$v_{R_c} = \frac{2D_j}{d_c} \cdot \frac{\tilde{c}_l^j - c_l^j}{\tilde{c}_l^j - \tilde{c}_c^j} \cdot \ln^{-1}\left(\frac{d_{\max}}{d_c}\right) \quad [2]$$

where $d_{\max}$ is the maximal diameter available for cylindrical growth, d_c is the diameter of columnar dendrite

trunks, and $\tilde{c}_c^j$ is the equilibrium mass fraction of the columnar solid at the liquid-solid interface. The maximal diameter can be chosen as $d_{\max} = 0.577 \cdot \lambda_1$ considering a hexagonal dendrite arrangement with dendrite arm spacing λ_1. This condition assumes that the entire residual melt is exactly consumed by the growing cylinder when it has reached its maximum diameter $d_{\max}$. In that case, when the melt convection is strong, Eqs. [1] and [2] have to be modified by including the Sherwood number.[10] Knowing the growth velocity of the equiaxed grain from Eq. [1], the mass-transfer rate from the liquid to equiaxed phase can be defined as

$$M_{le} = v_{R_e} \cdot (n \cdot \pi \cdot d_e^2) \cdot \rho_e \cdot f_{\mathrm{imp}} \quad [3]$$

which is the product of the growth velocity, the total surface area of spherical grains, the ρ_e density of the equiaxed phase, and the impingement factor. Also, knowing the growth velocity for columnar dendrite trunks from Eq. [2], the mass-transfer rate from the liquid to columnar phase can be defined as

$$M_{lc} = v_{R_c} \cdot \left(\frac{2\sqrt{3} \cdot \pi \cdot d_c}{3\lambda_1^2}\right) \cdot \rho_c \cdot f_{\mathrm{imp}} \quad [4]$$

where ρ_c is the density of the columnar phase. The impingement factors in Eqs. [3] and [4] are different for the spherical and cylindrical growth. For equiaxed solidification, the Avrami-type impingement factor is used ($f_{\mathrm{imp}} = f_l$). For the definition of the columnar impingement factor, we assume a linear decrease of it with diameter for those trunks which that have a larger diameter than the dendrite arm spacing.

$$f_{\mathrm{imp}} = \begin{cases} 1, & 0 < d_c \leq \lambda_1, \\ 1 - \dfrac{d_c - \lambda_1}{d_{\max} - \lambda_1}, & \lambda_1 < d_c \leq d_{\max} \end{cases} \quad [5]$$

B. Thermodynamics and Ternary System

The volume averaged and equilibrium mass fractions of species $c_l^j, \tilde{c}_l^j, \tilde{c}_e^j, \tilde{c}_c^j$ for the estimation of growth velocities are computed by solving a nonlinear algebraic system of equations with a Newton-type method. The process-related quantities c_l^j and the bulk temperature T_l are coupled with the liquid-solid interfacial quantities $\tilde{c}_l^j, \tilde{c}_e^j, \tilde{c}_c^j$.[14] Figure 1 shows the occurring phases for the iron-rich corner of the ternary (Fe-C-Cr) phase diagram, which is based on the Thermo-Calc calculations. For the solidification simulation, the ferrite and austenite areas are of special interest.

The liquidus surface and the solubilities for carbon and chromium for this region were calculated, as shown in Figure 2. The initial concentration of 0.3 wt pct carbon 15.0 wt pct chromium and Fe in balance of the investigated steel is shown as point A in Figure 2.

The liquidus temperature, carbon, and chromium solubility during solidification are approximated by their linearizations around the initial concentration point A, which are valid for the ferritic region, and
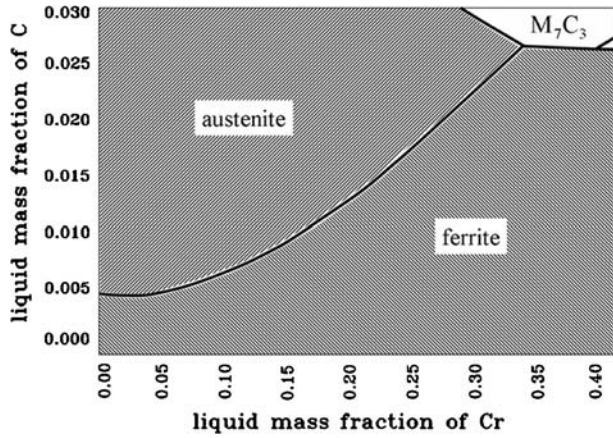
Fig. 1—Primary solid phases forming from the melt in the Fe-rich corner of the ternary Fe-C-Cr system estimated from Thermo-Calc calculations.
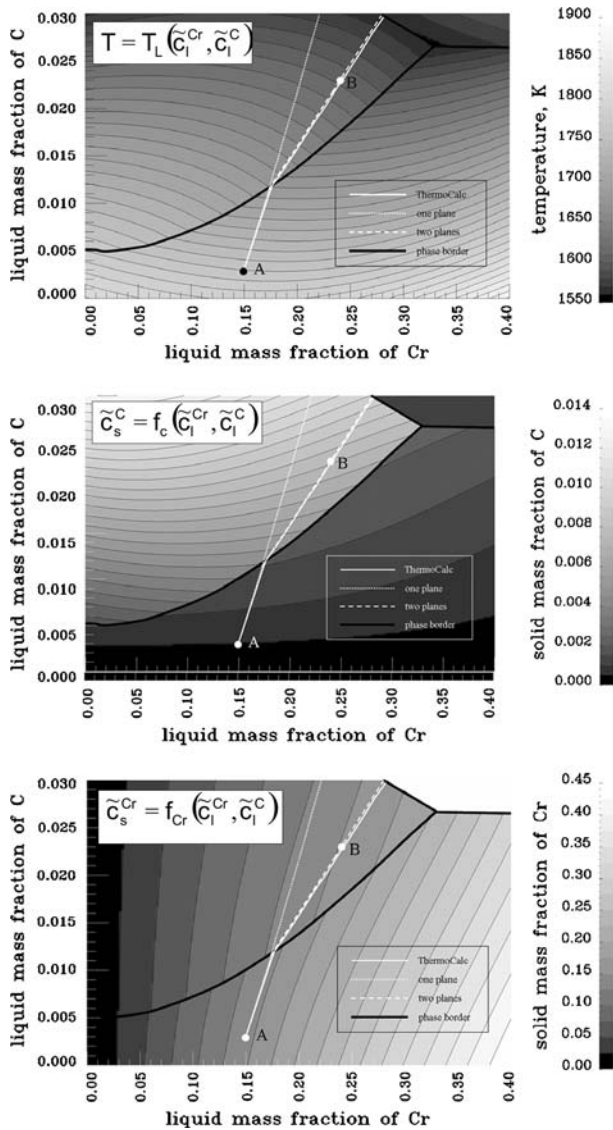

Fig. 2—Contour plots for the liquidus surface and solubility for carbon and chromium in the solid phase.

around point B, which are valid for the austenitic region. Point B was chosen after estimating the solidification path for this alloy using Thermo-Calc-Scheil solidification simulation. The consideration of point B is necessary in order to take the peritectic solidification into account, which occurs for the investigated steels.

C. Governing Equations

The multiphase Eulerian–Eulerian approach is used to obtain the mass, momentum, enthalpy, and species conservations. For solidification, the conservation of mass for each phase is described by

$$\frac{\partial}{\partial t}(f_l \rho_l) + \nabla \cdot (f_l \rho_l \mathbf{u}_l) = -M_{le} - M_{lc} \qquad [6]$$

$$\frac{\partial}{\partial t}(f_e \rho_e) + \nabla \cdot (f_e \rho_e \mathbf{u}_e) = M_{le} \qquad [7]$$

$$\frac{\partial}{\partial t}(f_c \rho_c) + \nabla \cdot (f_c \rho_c \mathbf{u}_c) = M_{lc} \qquad [8]$$

where f_i is the volume fraction of the corresponding phase. During the ingot casting process, the melting occurs when the mass-transfer rate from a solid (columnar or equiaxed) phase to the liquid phase becomes negative. In this case, the source terms $M_{lc}(=-M_{cl})$ and $M_{le}(=-M_{el})$ are the mass-transfer rate (kg/m^3/s) from the liquid to the columnar phase and from the liquid to the equiaxed phase. The fragmentation and attachment are not considered in the model; therefore, the mass-transfer rate M_{ce} from columnar to equiaxed phase is neglected.

The momentum conservation equations are solved for the melt and the equiaxed phase. Thermal and solutal buoyancy are modeled using the Boussinesq approach. The momentum exchange terms have two parts. One of them is due to phase transformation and the other one is due to drag force. Momentum exchange between columnar and equiaxed phase is taken into account when the local volume fraction of columnar phase reaches a critical value ($f_c = 0.2$). In this case, the drag force coefficient between columnar and equiaxed phase is set to an infinite value and the equiaxed grains are captured in the columnar front. Otherwise, the drag force coefficient is set to zero and the solid phases do not interact in terms of motion. The momentum conservation equation for the liquid phase is given by

$$\frac{\partial}{\partial t}(f_l \rho_l \mathbf{u}_l) + \nabla \cdot (f_l \rho_l \mathbf{u}_l \otimes \mathbf{u}_l)$$

$$= f_l \rho_l^{\mathrm{ref}} \left[1 - \beta_T(T_l - T^{\mathrm{ref}}) - \sum_{i=1}^{n} \beta_c^j (c_l^j - c^{\mathrm{ref}}) \right] \mathbf{g} - f_l \nabla p$$

$$+ \nabla^2(\mu_l f_l \mathbf{u}_l) + \frac{1}{3}\nabla(\nabla \cdot \mu_l f_l \mathbf{u}_l) - \mathbf{u}_l(M_{le} + M_{lc})$$

$$- K_{le}(\mathbf{u}_l - \mathbf{u}_e) - K_{lc}(\mathbf{u}_l - \mathbf{u}_c) \qquad [9]$$

Also, for the melting process, the following momentum equation is valid for the liquid phase:

$$\frac{\partial}{\partial t}(f_l\rho_l\mathbf{u}_l) + \nabla\cdot(f_l\rho_l\mathbf{u}_l \otimes \mathbf{u}_l)$$

$$= f_l\rho_l^{\mathrm{ref}}\left[1 - \beta_T(T_l - T^{\mathrm{ref}}) - \sum_{i=1}^{n}\beta_c^j(c_l^j - c^{\mathrm{ref}})\right]\mathbf{g} - f_l\nabla p$$

$$+ \nabla^2(\mu_l f_l\mathbf{u}_l) + \frac{1}{3}\nabla(\nabla\cdot\mu_l f_l\mathbf{u}_l) + \mathbf{u}_e M_{el} + \mathbf{u}_c M_{cl}$$

$$+ K_{el}(\mathbf{u}_e - \mathbf{u}_l) + K_{cl}(\mathbf{u}_c - \mathbf{u}_l) \quad [10]$$

where $\mathbf{u}_l$, $\mathbf{u}_e$, $\mathbf{u}_c$ are the velocities of the liquid, equiaxed, and columnar phases, respectively; $\mathbf{g}$ is the gravity acceleration; p is the scalar pressure field; μ_l is the dynamic viscosity of the liquid; and $K_{el}(=k_{le})$ and $K_{cl}(=k_{lc})$ are drag coefficients among the phases. The $\rho_l^{\mathrm{ref}}, T_l^{\mathrm{ref}}, c_l^{\mathrm{ref}}$ quantities are the corresponding density, temperature, and species reference values, respectively; β_T is thermal expansion coefficient; and β_c^j is the solutal expansion coefficient of the jth species. The momentum conservation equation for the equiaxed phase is given by

$$\frac{\partial}{\partial t}(f_e\rho_e\mathbf{u}_e) + \nabla\cdot(f_e\rho_e\mathbf{u}_e \otimes \mathbf{u}_e)$$

$$= f_e\left[\rho_e^{\mathrm{ref}} + (\rho_e - \rho_l)\right]\mathbf{g} - f_e\nabla p + \nabla^2(\mu_e f_e\mathbf{u}_e)$$

$$+ \frac{1}{3}\nabla(\nabla\cdot\mu_e f_e\mathbf{u}_e) + \mathbf{u}_l M_{le} + K_{le}(\mathbf{u}_l - \mathbf{u}_e)$$

$$+ K_{ce}(\mathbf{u}_c - \mathbf{u}_e) \quad [11]$$

Also, for the melting process, we can derive the following conservation equation:

$$\frac{\partial}{\partial t}(f_e\rho_e\mathbf{u}_e) + \nabla\cdot(f_e\rho_e\mathbf{u}_e \otimes \mathbf{u}_e)$$

$$= f_e\left[\rho_e^{\mathrm{ref}} + (\rho_e - \rho_l)\right]\mathbf{g} - f_e\nabla p + \nabla^2(\mu_e f_e\mathbf{u}_e)$$

$$+ \frac{1}{3}\nabla(\nabla\cdot\mu_e f_e\mathbf{u}_e) - \mathbf{u}_e M_{el} - K_{el}(\mathbf{u}_e - \mathbf{u}_l)$$

$$- K_{ec}(\mathbf{u}_e - \mathbf{u}_c) \quad [12]$$

where μ_e is the dynamic viscosity of equiaxed phase, $\Delta\rho_e$ is the density difference between the equiaxed and liquid phase, and $K_{le}(=k_{el})$ and $K_{ce}(=k_{ec})$ are the drag coefficients among the phases. The columnar dendrite trunks grow from the mold wall into the bulk melt, and an advanced method is applied for tracking the columnar tip envelope. The tip growth velocity is taken into account when the local volume fraction of equiaxed grains f_e becomes larger than a predefined critical threshold. The Lipton–Glicksman–Kurz[15] model has been further developed for ternary systems, but the details will be discussed in a future article.

The enthalpy conservation equations for the different phases are given by

$$\frac{\partial}{\partial t}(f_l\rho_l h_l) + \nabla\cdot(f_l\rho_l\mathbf{u}_l h_l)$$

$$= \nabla\cdot(f_l k_l\nabla T_l) - h_l\cdot(M_{le} + M_{lc})$$

$$- H^*[(T_l - T_e) + (T_l - T_c)] \quad [13]$$

$$\frac{\partial}{\partial t}(f_e\rho_e h_e) + \nabla\cdot(f_e\rho_e\mathbf{u}_e h_e)$$

$$= \nabla\cdot(f_e k_e\nabla T_e) + h_l M_{le} + H^*[(T_l - T_e) - (T_e - T_c)] \quad [14]$$

$$\frac{\partial}{\partial t}(f_c\rho_c h_c) + \nabla\cdot(f_c\rho_c\mathbf{u}_c h_c)$$

$$= \nabla\cdot(f_c k_c\nabla T_c) + h_l M_{lc} + H^*[(T_l - T_c) + (T_e - T_c)] \quad [15]$$

where the enthalpies are defined as $h_l = \int_{T_{\mathrm{ref}}}^{T_l} c_{p(l)}dT + h_l^{\mathrm{ref}}$ and $h_e = h_c = \int_{T_{\mathrm{ref}}}^{T_e} c_{p(s)}dT + h_e^{\mathrm{ref}}$, with $c_{p(l)}$ and $c_{p(s)}$ being the specific heat of the liquid and solid phases, respectively; and T_{ref} and $h_l^{\mathrm{ref}}, h_e^{\mathrm{ref}}$ are the corresponding reference values. The k_l, k_e, k_c quantities are the thermal conductivities for each phase; H^* is the heat-transfer coefficient between the phases; and T_l, T_e, T_c are the corresponding temperatures of the phases, which are assumed to be equal. During melting, the direction of the process will be changed. Therefore, the mass-transfer rates from the liquid to columnar phase $M_{lc}(=-M_{cl})$ and from the liquid to equiaxed phase $M_{le}(=-M_{el})$ will be different in their signs, and we have to take into account the corresponding h_e, h_c enthalpy values as coefficients instead of the h_l liquid enthalpy.

The numerically accurate solution of the species transport equations provides trustable results for the predicted macrosegregation field at the end of solidification. The thermodynamic-related quantities $\tilde{c}_l^j, \tilde{c}_e^j, \tilde{c}_c^j$ in the right-hand side of the species transport equations are computed from the corresponding (Fe-C-Cr) phase diagram information. The species conservation equations for the different phases are given by

$$\frac{\partial}{\partial t}(f_l\rho_l c_l^j) + \nabla\cdot(f_l\rho_l\mathbf{u}_l c_l^j) = -\tilde{c}_e^j M_{le} - \tilde{c}_c^j M_{lc} \quad [16]$$

$$\frac{\partial}{\partial t}(f_e\rho_e c_e^j) + \nabla\cdot(f_e\rho_e\mathbf{u}_e c_e^j) = \tilde{c}_e^j M_{le} \quad [17]$$

$$\frac{\partial}{\partial t}(f_c\rho_c c_c^j) + \nabla\cdot(f_c\rho_c\mathbf{u}_c c_c^j) = \tilde{c}_c^j M_{lc} \quad [18]$$

where c_l^j, c_e^j, c_c^j are the mass fractions of the jth species. The mixture concentration c_{mix}^j is obtained by an auxiliary quantity in order to study the macrosegregation quantitatively:

$$c_{\mathrm{mix}}^j = \frac{c_l^j\cdot\rho_l^j\cdot f_l^j + c_e^j\cdot\rho_e^j\cdot f_e^j + c_c^j\cdot\rho_c^j\cdot f_c^j}{\rho_l^j\cdot f_l^j + \rho_e^j\cdot f_e^j + \rho_c^j\cdot f_c^j} \quad [19]$$

For the computation of the mass-transfer rate from liquid to equiaxed phase in Eq. [3], the conservation of the number density n of the equiaxed grains is described by the following equation:

$$\frac{\partial n}{\partial t} + \nabla\cdot(\mathbf{u}_e n) = \frac{d(\Delta T)}{dt}\cdot\frac{n_{\max}}{\sqrt{2\pi}\cdot\Delta T_\sigma}\cdot e^{-\frac{1}{2}\left(\frac{\Delta T - \Delta T_N}{\Delta T_\sigma}\right)^2} \quad [20]$$

where n_{max} is the maximal available nucleation sites, ΔT is the constitutional undercooling, ΔT_N is the undercooling for maximum grain production rate, and ΔT_σ is the Gaussian distribution width of the nucleation law. This approach, originally developed by Oldfield, suggests a continuous rather than a discrete distribution of nucleation sites.[7,13,16]

The mass, momentum, energy, and species conservation equations for each phase have been implemented in the commercial finite volume method based FLUENT-ANSYS v6.3 code using user-defined functions. Further details about the multiphase volume averaging model can be found in References 9 through 14.

III. CAST BENCHMARK INGOT AND BOUNDARY CONDITIONS

In order to validate the results of the numerical models, three stainless steel ingots (Fe-0.3 wt pct C-14.82 wt pct Cr) with an approximate weight of 32 kg each were cast in a laboratory induction furnace. The melt was built up with pure iron, carbon, and ferrochromium in an induction furnace.

The presence of trace elements such as sulfur or phosphorus are neglected in the analysis. The last temperature measurement of the melt before casting revealed 1555 °C, which was taken as an initial temperature for solidification simulation. The laboratory furnace only allowed downhill casting. In this experiment, a big end up gray cast mold was used. The mold was placed on a heavy gray cast bottom plate and was instrumented with thermocouples (TCs) of TypeN in different heights and different depths of the mold wall. Additionally, one thermocouple of TypeS was installed into the casting to measure the melt temperature and the cooling behavior of the ingot.

Figure 3 shows a sketch of the casting system. The blue colored "X" in Figure 3 shows the position of the melt TC, which was housed in a refractory tube and inserted from below *via* a drill hole in the bottom plate. The red colored X's show the TCs positioned 5 mm behind the inner mold wall, and the green colored X's show the position of the surface TCs. After the casting process was complete, casting powder was given on top of the liquid steel to reduce the amount of shrinkage cavities. The measured cooling curves are shown in Figure 4.

Based on the temperature measurements shown in Figure 4, the heat-transfer coefficient for the contact area between the ingot and mold wall was estimated by an inverse simulation using the finite elements method (FEM) software package calco*soft*2D (Calcom ESI, Lausanne, Switzerland). Normally, the heat-transfer coefficient is process dependent. For the time period when the melt is in perfect contact with the mold, the heat transfer is relatively high. Due to the casting shrinkage, an air gap forms between the casting and the mold, leading to a lower heat transfer. An average value of 700 W/(m² K) was used for the ingot/mold and the ingot/bottom plate boundaries, representing the overall
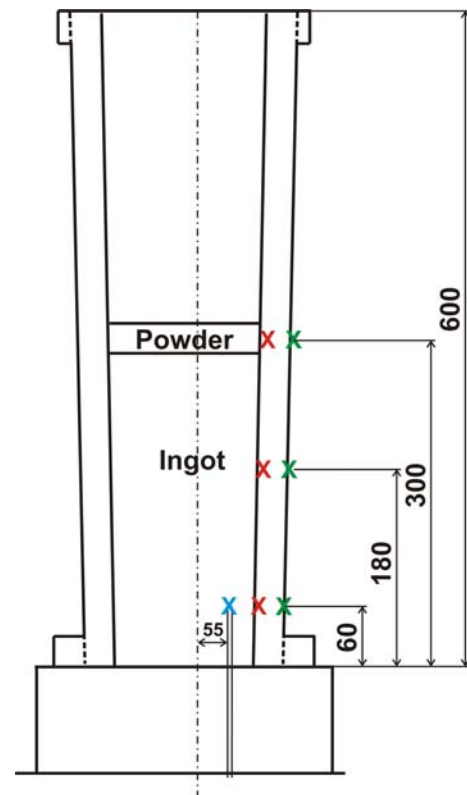

Fig. 3—Sketch of the casting setup showing the positions of the thermocouples in the mold and in the solidifying ingot.
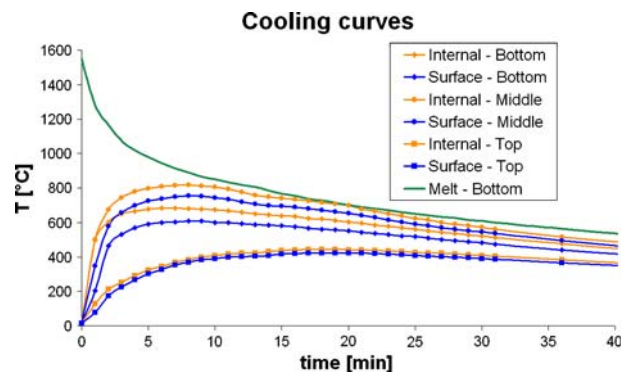

Fig. 4—Measured cooling curves showing the time-temperature readings from the solidifying melt (green) and the mold at different heights and depths (blue and orange).

process. The heat-transfer coefficient at the top was estimated with 100 W/(m² K). The heat transfer in the upward direction is lower due to the insulation powder, which was added on top of the ingot. This fact is also reflected in the temperature curves. The two lines (internal-top and surface-top) were measured in the height of the casting powder, and they exhibit the lowest temperature readings. The geometry in the simulation was two-dimensional axisymmetric. Mold filling was not considered. Solidification simulation starts with an initial temperature of 1555 °C, which was experimentally determined.

IV. RESULTS AND DISCUSSION

The cast ingot was cut in half along the center axis. Chemical analysis was performed on one half of the ingot for 20 points in total distributed over four heights. The macrosegregation distribution patterns of all three ingots are similar. The representative result for the carbon and chromium distribution is depicted in Figure 5.

The measuring errors were 0.01 wt pct for carbon and 0.05 wt pct for chromium. The measured result shows that the amount of macrosegregation of carbon is very close to the measuring error. Due to this fact, the macrosegregation of carbon cannot be considered as significant in contrary to the macrosegregation of chromium, which well exceeds the measuring error.

The observed amount of macrosegregation is very small. It can be explained by the comparatively low ingot weight and the high heat flow, which results in high solidification velocity. The other half of the ingot was etched to reveal the primary solidification structure, which is shown in Figure 6.

Although the top of the cast ingot was insulated, a thin solidified cap evolved in the early stages of solidification, sealing the ingot off. Therefore, the feeding flow was significantly hindered. As a result, the upper third part of the benchmark ingot is occupied by a shrinkage cavity (shaded area in Figure 6). This area was neglected for the model validation. The sound area of the ingot shows the expected columnar and equiaxed phases. Additional examination with light-optical microscopy was performed in order to affirm the drawn phase border lines in Figure 6. It should be mentioned that one should only derivate a trend in terms of solidification morphology from this figure, because there is no sharp edge between the different growth morphologies.

Figure 7 shows the results for carbon and chromium distribution from the simulation. The amount of computed macrosegregation is very small, which coincides with the measured results from the experiment.

The results for primary structure formation are shown in Figure 8. The model, however, neglects the formation of shrinkage cavities in castings. The liquid and equiaxed phases are free to move. The consideration of this

equiaxed phase is crucial in order to simulate the equiaxed grain sedimentation, which is responsible for the negative segregated bottom zones of steel ingots. Next to the mold walls and in the bottom region, a high amount of equiaxed phase had been calculated. The model assumes columnar dendrites growing from the mold wall toward the bulk melt against the direction of the heat flow. In the early stages of solidification, however, equiaxed grains can nucleate in this region because of the high heat transfer in the mold. This phenomenon is termed in the literature as the "equiaxed
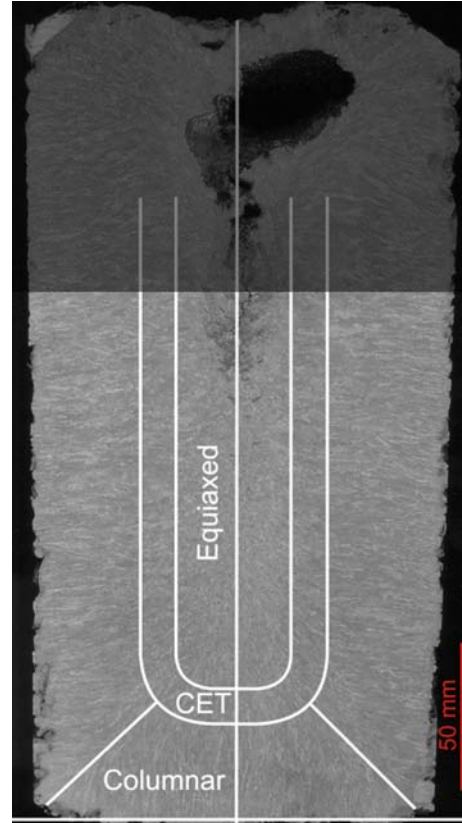
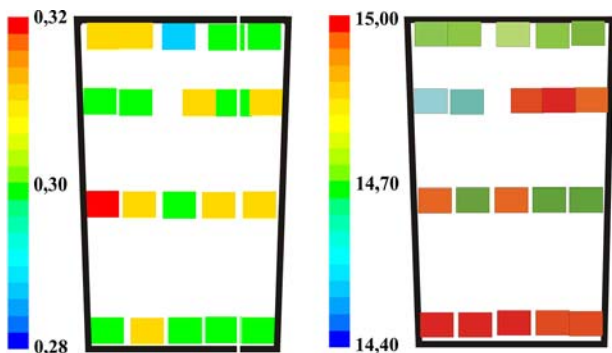Fig. 6—Macroetching of the ingot with marked out areas of different growth morphologies.

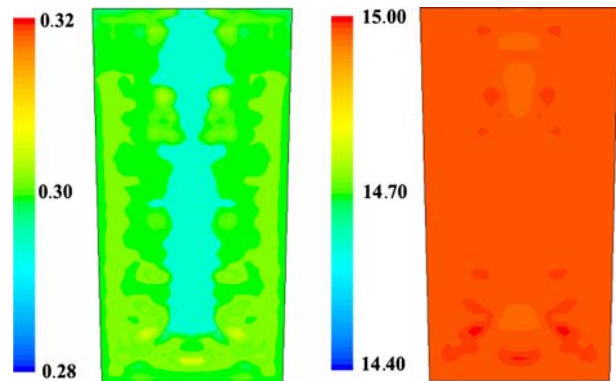Fig. 5—Chemical analysis of carbon (left) and chromium (right) in weight percent.

Fig. 7—Simulation results of the carbon (left) and chromium (right) distribution in weight percent.
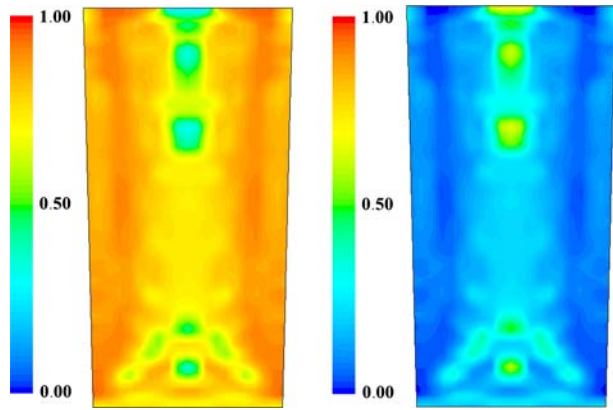
Fig. 8—Simulation results of the primary solid phase distribution: (left) volume fraction of columnar phase and (right) volume fraction of equiaxed phase.

chill zone." Due to the bad surface quality of the laboratory ingot, this particular zone could not be accounted for in the casting experiment. In Figure 8, it is also clearly visible that the columnar structure dominates over the entire casting, and the amount of equiaxed phase appears to be somewhat higher in the center, which matches the experiment results in general. High volume fractions of equiaxed phase are pronounced in the bottom area of the computed ingot as a result of the sedimentation of equiaxed grains. Nucleation of equiaxed grains is described in this model with a Gaussian function,[9,10,12,13] where the nucleation behavior is dependent of three parameters. The mean undercooling ΔT_N was set to 30 K, the standard deviation ΔT_σ to 15 K, and the maximum number density of grains was chosen to be $n_{max} = 10^9$ m^{-3}. The shown results are the first outcomes of the multiphase solidification simulation in combination with the ternary thermodynamic information.

V. SUMMARY

The method of combining ternary phase diagram information with multiphase solidification simulation described in References 10 and 14 was used. A multiphase model for prediction of macrosegregation and the primary solidification structure was evaluated by comparison of the numerical simulation results with the experimental data. Small laboratory scale ingots with ternary alloy (Fe-C-Cr) were cast and simulated. Good agreement was found in the overall segregation pattern. The predicted macrostructure follows the trend that was found in an experimental casting as well.

Although the potential of the model to simulate the solidification behavior of steel ingots was verified, further steps are necessary to determine and justify the equiaxed grain number density, the parameters for the tip velocity of columnar phase, and the drag coefficient between phases.

Furthermore, this study is going to be extended to the ingots of larger scale. In the industry scale ingots, the multiphase flow phenomena during solidification would be different; hence, the amount of macrosegregation is expected to be much more serious than we observed in the laboratory scale ingots. The effect of the shrinkage cavity should also be considered in future model development.

REFERENCES

1. M.C. Flemings: *Solidification Processing*, McGraw-Hill, New York, NY, 1974, pp. 214–58.
2. G. Lesoult: *Mater. Sci. Eng.*, 2005, vols. A413–A414, pp. 19–29.
3. M.C. Flemings: *ISIJ Int.*, 2000, vol. 40, pp. 833–41.
4. H. Combeau, J.M. Drezet, A. Mo, and M. Rappaz: *Metall. Mater. Trans. A*, 1996, vol. 27A, pp. 2314–27.
5. C. Beckermann: *Mater. Rev.*, 2002, vol. 47 (5), pp. 243–61.
6. J.P. Gu and C. Beckermann: *Metall. Mater. Trans. A*, 1999, vol. 30A, pp. 1357–66.
7. Th. U. Kaempfer and M. Rappaz: *Proc. MCWASP–IX*, Aachen, Germany, Shaker Verlag, Aachen, 2000, pp. 640–45.
8. H. Cao, H. Shen, and B. Liu: *Proc. MCWASP–XI*, Opio, France, TMS, Warrendale, 2006, pp. 219–26.
9. A. Ludwig and M. Wu: *Mater. Sci. Eng.*, 2005, vols. A413–A414, pp. 109–14.
10. A. Ludwig, A. Ishmurzin, M. Gruber-Pretzler, F. Mayer, M. Wu, R. Tanzer, and W. Schützenhöfer: *Proc. SP07*, The University of Sheffield, Sheffield, United Kingdom, 2007, pp. 493–96.
11. M. Wu and A. Ludwig: *Metall. Mater. Trans. A*, 2006, vol. 37A, pp. 1613–31.
12. M. Wu and A. Ludwig: *Metall. Mater. Trans. A*, 2007, vol. 38A, pp. 1465–75.
13. L. Könözsy, F. Mayer, A. Ishmurzin, A. Kharicha, M. Wu, A. Ludwig, R. Tanzer, and W. Schützenhöfer: *Proc. ASMET–STEELSIM*, Seggau, Austria, Gutenberghous Druck, Knittelfeld, 2007, pp. 126–32.
14. A. Ishmurzin, M. Gruber-Pretzler, F. Mayer, M. Wu, and A. Ludwig: *IJMR Int.*, 2008, vol. 99, pp. 618–25.
15. J. Lipton, M.E. Glicksman, and W. Kurz: *Mater. Sci. Eng.*, 1984, vol. 65, pp. 57–63.
16. W. Oldfield: *ASM Trans.*, 1966, vol. 59, pp. 945–61.